

Tightly Joined Positioning and Control Model for Unmanned Aerial Vehicles Based on Factor Graph Optimization

Peiwen Yang, Weisong Wen*, *Member, IEEE*, Shiyu Bai, *Member, IEEE*, and Li-Ta Hsu, *Senior Member, IEEE*

Abstract— The execution of flight missions by unmanned aerial vehicles (UAV) primarily relies on navigation. In particular, the navigation pipeline has traditionally been divided into positioning and control, operating in a sequential loop. However, the existing navigation pipeline, where the positioning and control are decoupled, struggles to adapt to ubiquitous uncertainties arising from measurement noise, abrupt disturbances, and nonlinear dynamics. As a result, the navigation reliability of the UAV is significantly challenged in complex dynamic areas. For example, the ubiquitous global navigation satellite system (GNSS) positioning can be degraded by the signal reflections from surrounding high-rising buildings in complex urban areas, leading to significantly increased positioning uncertainty. An additional challenge is introduced to the control algorithm due to the complex wind disturbances in urban canyons. Given the fact that the system positioning and control are highly correlated with each other, this research proposes a tightly joining positioning and control model (JPCM) based on factor graph optimization (FGO). In particular, the proposed JPCM combines sensor measurements from positioning and control constraints into a unified probabilistic factor graph. Specifically, the positioning measurements are formulated as the factors in the factor graph. In addition, the model predictive control (MPC) is also formulated as the additional factors in the factor graph. By solving the factor graph contributed by both the positioning-related factors and the MPC-based factors, the complementarity of positioning and control can be deeply exploited. Finally, we validate the effectiveness and resilience of the proposed method using a simulated quadrotor system which shows significantly improved trajectory following performance. To benefit the research community, we open-source our code and make it available at https://github.com/RoboticsPolyu/IPN_MPC.

Index Terms— Positioning; Model predictive control (MPC); Dynamic model; Factor graph optimization (FGO); Joint optimization; Positioning uncertainty, Unmanned aerial vehicles (UAV).

I. INTRODUCTION

The pipeline of decoupling positioning and control has dominated the practice of UAV for decades: Reliable navigation is of great significance for the applications of unmanned aerial vehicles (UAV) [1-5]. Typically, the navigation pipeline has traditionally been divided into positioning and control, operating in a sequential loop [6, 7].

The authors are with the Department of Aeronautical and Aviation Engineering, Polytechnic University, Hong Kong, E-mail: peiwenl.yang@connect.polyu.hk; welson.wen@polyu.edu.hk; shiyu.bai@polyu.edu.hk; lt.hsu@polyu.edu.hk. (Corresponding author: Weisong Wen.)

The positioning can be achieved using sensors, such as the global navigation satellite system (GNSS) receivers [8, 9]. Then the state estimation from the positioning module is fed to the controller of the UAV, such as the popular model predictive control (MPC) [10]. The practice of decoupled positioning and control has become a classical pipeline of autonomous systems for years.

Positioning solutions can be challenged with large uncertainty in complex scenes: In particular, the positioning can be derived from the state estimator, such as the Kalman filter [11, 12] or factor graph optimization (FGO) [13, 14] based on the onboard sensors. For example, GNSS was widely used in vehicular localization under open sky and usually combined with proprioceptive sensors such as inertial measurement unit (IMU) and exteroceptive sensors such as light detection and ranging (LiDAR) during satellite signal outages [9, 15-20]. However, the performance of these solutions relies strongly on the environmental conditions [21-23]. On the one hand, the GNSS positioning can be significantly degraded in urban canyons due to the multipath effects caused by the signal reflections from high-rise buildings [23]. Although numerous works were proposed to mitigate the impacts of the GNSS outliers [23, 24], the positioning solution derived from the GNSS is still unreliable in highly urbanized areas with significant uncertainty. Moreover, the LiDAR-based positioning can also be significantly challenged in urban canyons due to the excessive dynamic objects [25], leading to unacceptable positioning uncertainty.

Insufficient awareness of the positioning uncertainty can challenge the controllers in complex scenes: Usually, the positioning solution is directly fed to the controller, such as the PID controller [26], assuming a perfect positioning accuracy is guaranteed. Unfortunately, positioning accuracy is usually not guaranteed in complex scenes using the existing GNSS or multi-sensory integration [9, 15-20]. As a result, the controller would inevitably lead to non-optimal control commands, therefore causing dangerous UAV actions. Hence, the control stability under large positioning uncertainty is essential for safety. The traditional control methods struggle to simultaneously deal with the uncertainty of state [27], obstacles [28], and nonlinear dynamics in the context of decoupling the positioning and control modules [29]. Instead of carefully coping with the uncertainty arising from the positioning module, the existing work [30, 31] mainly focuses on the disturbances of the dynamical model, while ignoring the uncertainties of raw measurements. In other words, positioning uncertainty is also considered a potential

disturbance from the environment. However, it is difficult to reliably distinguish the positioning uncertainty and the exact disturbance coming from the surrounding environments. To effectively consider the uncertainty of the positioning module, researchers proposed to directly add the positioning uncertainty as the covariance matrix of the cost function in the MPC [32, 33], which has attracted lots of attention recently. However, the work in [32, 33] has several key drawbacks: (1) it relied heavily on the reliability of the uncertainty provided by the positioning module, which is hard to obtain in complex scenes as mentioned above. (2) the information from the controller cannot flow back to the positioning modules. For example, the dynamics of the UAV system applied in the controller can also contribute to the positioning modules [34, 35]. In other words, the positioning modules and the controller are highly complementary and correlated with each other. *Why do we decouple the positioning and control module?* Interestingly, the work from Prof. Frank Dellaert, from the School of Interactive Computing at the Georgia Institute of Technology, U.S., proposed a control and planning joint model [36] for robotics, in a tightly coupled manner. To enable efficient information flow between the positioning and control module, the path planning and control problems are formulated as a combined problem using the factor graph. As a result, the uncertainty from both the path planning and the control can be considered optimally and simultaneously. The work [37] also reformulated the measurements over a fixed time window into an optimal control problem instead of a single measurement for the estimation at each time step. Similar work was done in equality and inequality-constrained optimal control [38, 39], and kinematic and dynamics problems for multi-body systems [40], which were solved by factor graphs [6]. Besides, some works [41, 42] tightly integrated trajectory estimation and path planning by utilizing obstacle avoidance factors and goal factors. The above papers revealed the feasibility of applying factor graphs to trajectory planning or control. All these exciting works inspire us with a question: *can we design a tightly coupled model to solve the positioning and control problems simultaneously?*

Inspired by the work in [36], this paper proposed a tightly joined positioning and control model (JPCM) that allows unifying the positioning and control under the same mathematics representation. Therefore, the primary aim is to tightly formulate a unified problem of positioning and control. Fortunately, the factor graph is investigated that can be used to construct the same mathematics representation for both positioning [43, 44] and control. Finally, the JPCM is evaluated by a well-designed quadrotor simulator, which considers the impact of aerodynamic drag force and the actuator's dynamic [45]. The results demonstrate the feasibility of the joining model and significantly improve trajectory tracking accuracy and success rate compared to nominal MPC methods, particularly under conditions characterized by significant state uncertainty. Moreover, the JPCM exhibits robust resilience. Concisely, after encountering rapid motion or serious observation errors, the controller will not exhibit excessive feedback and can slowly change in its original state. Resilience is a critical feature, as it ensures the stability of the system even in adverse conditions. We believe

that the tightly JPCM, proposed in this paper, would be a profound framework that is expected to be applied to multi-sensor integrated autonomous systems under complex environments.

Specifically, the main contributions of this paper include:

(1) *Propose a tightly coupled model to solve navigation problems, which combines positioning constraints and control constraints into a singular quadratic optimization problem.* The proposed approach formulates a tightly coupled joint positioning and control model that effectively addresses the navigation challenges due to positioning and dynamics uncertainty.

(2) *Formulate the tightly joined positioning and control model through the probability factor graph.* We categorize measurements into absolute factors, such as the GNSS factor, and relative factors, like the LiDAR scan-matching factor. Additionally, we formulate dynamics, trajectory following, and control input constraints as control-based factors. Further considering the aerodynamic drag effect in the dynamics model, JPCM-drag is proposed to tackle the path following offset. All these factors are consolidated into a unified factor graph, which is then solved using GTSAM [13]. As a result, the uncertainty of state and nonlinear dynamics is coupled with the control law, bridging the gap between positioning and control.

(3) *Evaluate the proposed JPCM through simulations and open-source code.* Except for the uncertainty of sensors and dynamic processes, the sharp wind, aerodynamic drag, and actuator's time constant are also simulated. These elements add a layer of complexity and realism to our simulator, making it closer to the real system. Lastly, we have made the code open source to benefit the research community.

The structure of the paper is as follows. In Section II, we give an overview of the proposed model's pipeline. Section III introduces the UAV's dynamic model and uniformly formulates positioning and MPC using the same mathematical representation. A tight JPCM is proposed and solved in Section IV. In Section V, numerical experiments are conducted to evaluate the performance of the proposed model. Section VI discusses more details. Finally, the conclusion is summarized in Section VII.

II. OVERVIEW

As illustrated in Fig 1, the classical navigation framework's pipeline runs in cycles, first by estimating the state and then deriving a control input \mathbf{u}_{opt} based on MPC. However, in the proposed JPCM, the positioning cost function from sensor-based constraints and control cost function from MPC-based constraints are integrated into a tightly joined optimization problem. Both positioning and control of autonomous systems are fundamentally quadratic nonlinear optimization problems, although the control problem has additional equality and inequality constraints on variables to be optimized. Then, the joined cost function is converted into a unified factor graph. Finally, we solve the tightly joined FGO problem using the popular GTSAM [13] library. All the symbols used in the paper are recorded in Table I.

> REPLACE THIS LINE WITH YOUR MANUSCRIPT ID NUMBER (DOUBLE-CLICK HERE TO EDIT) <

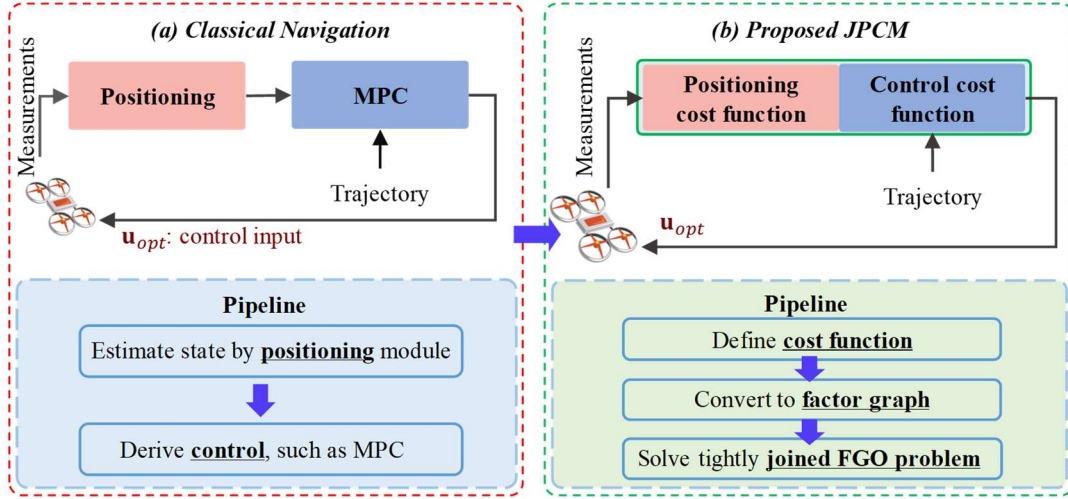


Fig. 1. The navigation pipeline: from (left) the classical model-based navigation to (right) the proposed tight JPCM. (a) The model-based navigation method has a fixed loop: estimating state and then deriving control. The positioning module and control module are decoupled. (b) The proposed JPCM integrates positioning and control into a cost function. Then, we convert the cost function to a probability factor graph, in which the positioning-related factors and MPC-based factors are tightly combined. More details on the joined factor graph are discussed in Section IV.

Table I. List of symbols

Symbol	Remarks
θ^\times , $\theta = [\theta_1 \ \theta_2 \ \theta_3]^T$	$\theta^\times = \begin{bmatrix} 0 & -\theta_3 & \theta_2 \\ \theta_3 & 0 & -\theta_1 \\ -\theta_2 & \theta_1 & 0 \end{bmatrix}$
$\mathbf{x} = [\mathbf{p}^T, \theta^T, \mathbf{v}^T, \omega^T]^T$	State \mathbf{x} , position \mathbf{p} , rotation $\mathbf{R} = \exp(\theta^\times)$, velocity \mathbf{v} , and angular speed ω
$\hat{\mathbf{x}}$	Optimized state
$\Delta \mathbf{x}$	State increment w.r.t initial state
$\delta \mathbf{x}$	State increment in the tangent space
\mathbf{z}	Sensor observation
\mathbf{u}	Control input
$\mathbf{z}^r, \mathbf{u}^r$	Reference state and reference input
$\boldsymbol{\tau} = [\mathbf{T}_b^T, \mathbf{M}_b^T]^T$	Resultant thrust \mathbf{T} and resultant torque \mathbf{M}
\mathbf{P}	Covariance matrix
\mathbf{K}	Control law
\mathbf{D}	Aerodynamic drag coefficient matrix
\mathbf{I}_b	Moment of inertia
g	Gravity constant
m_b	UAV's mass
c_t	Rotor's aerodynamic thrust coefficient
k_m	Rotor's aerodynamic torque coefficient
$\mathbf{p}_{r_j}^b$	j -th rotor's position in the body frame
$\mathbf{T}_{b_l}^w$	UAV's pose in the world frame at timestamp l
$\mathbf{T}_{l+1}^l, \mathbf{P}_l^l$	Relative pose transformation from timestamp l to timestamp $l+1$ and its covariance matrix
\mathbf{r}^R	Relative factor residuals
\mathbf{r}^A	Absolute factor residuals
\mathbf{r}^{ref}	Reference trajectory factor residuals
\mathbf{r}^D	Dynamic control factor residuals
\mathbf{r}^U	Control limit factor residuals
$\mathbf{h}(\mathbf{u}_j)$	Input constraint factor residuals
$\mathbf{Q}_k, \mathbf{Q}_N, \mathbf{R}_t, \mathbf{Q}_{lim}$	Weighting matrix in MPC; covariance matrix in JPCM
\mathbf{I}_n	n -dimensional unit vector

III. PROBLEM DESCRIPTION

Fig 2 demonstrates that both positioning (red box) and MPC (blue box) can be conceptualized as an optimization problem on-manifold. In the context of a canonical positioning model,

factors derived from measurements can be categorized into two distinct types [46]: absolute factors and relative factors. Absolute factors apply constraints to the robot's state at a specific moment, while relative factors constrain the variation between states at varying time intervals.

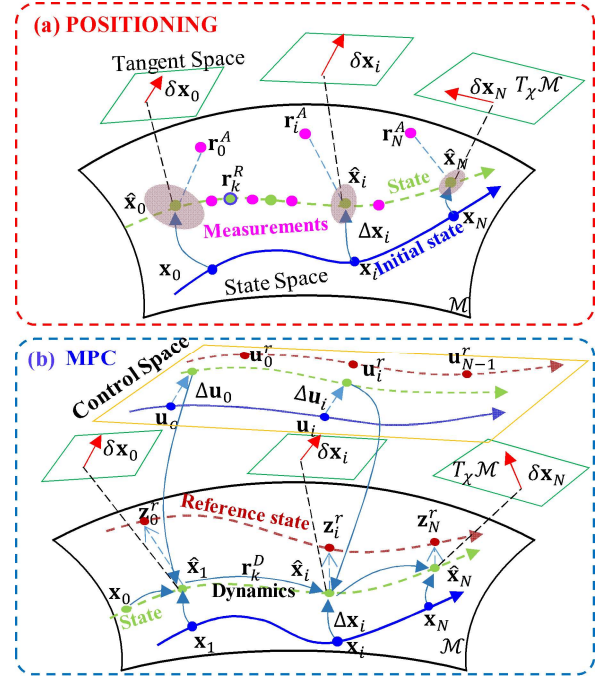


Fig. 2. The representation and linearization of the positioning and MPC problem can be unified, which implies the information of control can flow back to the positioning problem. (a) Positioning is a probability FGO problem with absolute factors \mathbf{r}^A and relative factors \mathbf{r}^R . (b) MPC can also be formulated as an FGO problem. Futural states are predicted by the dynamic model, hence the dynamic factors \mathbf{r}^D become the informational bridge.

As for the MPC in the blue box of Fig 9, starting from an initial state \mathbf{x}_0 , constraints derived from the pre-planned trajectory reference \mathbf{z}^r and the dynamic model collectively affect the adjustment of on-manifold variables. Therefore, we combine measurement-based factors and control-based constraints into a unified optimization problem. The UAV

dynamic model, positioning, and MPC are further explored in the following sections.

A. The UAV dynamic model

The generalization dynamics model [27, 47] of a UAV is as follows:

$$\dot{\mathbf{x}} = \mathbf{f}(\mathbf{x}, \boldsymbol{\tau}) \quad (1a)$$

$$\boldsymbol{\tau} = \mathbf{g}(\mathbf{u}) \quad (1b)$$

where $\mathbf{x} = [(\mathbf{p}_b^w)^T, (\boldsymbol{\theta}_b^w)^T, (\mathbf{v}_b^w)^T, (\boldsymbol{\omega}_b)^T]^T$ is the UAV's state that includes position \mathbf{p}_b^w , rotation $\mathbf{R}_b^w = \exp\{(\boldsymbol{\theta}_b^w)^\times\}$, velocity \mathbf{v}_b^w , and angular speed $\boldsymbol{\omega}_b$, and $\boldsymbol{\tau} = [\mathbf{T}_b^T, \mathbf{M}_b^T]^T$ represents the resultant thrust $\mathbf{T}_b \in \mathbb{R}^3$ and resultant torque $\mathbf{M}_b \in \mathbb{R}^3$, and $\mathbf{u} = [u_0, \dots, u_j, \dots, u_K]^T, K \geq 3, K \in \mathbb{N}$ is the control input vector, where u_j represents the angular speed of the j -th motor of the UAV. $\mathbf{f}(\ast)$ and $\mathbf{g}(\ast)$ represent the generalization dynamics model and control allocation model, respectively.

The continuous-time linearized dynamics of (1a) is as follows [27, 47]:

$$\begin{aligned} \dot{\mathbf{p}}_b^w &= \mathbf{v}_b^w \\ \dot{\mathbf{R}}_b^w &= \mathbf{R}_b^w \boldsymbol{\omega}_b^\times \\ \dot{\mathbf{v}}_b^w &= -\mathbf{R}_G^w \mathbf{e}_3 g + (\mathbf{R}_b^w \mathbf{T}_b + \mathbf{R}_b^w \mathbf{D} \mathbf{R}_w^b \mathbf{v}_b^w) / m_b \\ \dot{\boldsymbol{\omega}}_b &= \mathbf{I}_b^{-1} (-\boldsymbol{\omega}_b^\times \mathbf{I}_b \boldsymbol{\omega}_b + \mathbf{M}_b) \end{aligned} \quad (2)$$

where m_b is UAV's mass, $\mathbf{e}_3 = [0, 0, 1]^T$, g is the gravity constant, \mathbf{D} is the aerodynamic drag coefficient matrix [45], and $\boldsymbol{\omega}_b^\times$ represents an operator that spins a 3D vector $\boldsymbol{\omega}_b$ to a skew-symmetric as follows:

$$\boldsymbol{\omega}_b^\times = \begin{bmatrix} 0 & -\omega_3 & \omega_2 \\ \omega_3 & 0 & -\omega_1 \\ -\omega_2 & \omega_1 & 0 \end{bmatrix} \quad (3)$$

\mathbf{I}_b is the moment of inertia, which is usually regarded as a diagonal matrix:

$$\mathbf{I}_b = \text{diag}(I_b^1, I_b^2, I_b^3) \quad (4)$$

Every rotor can generate aerodynamic thrust $F = c_t u_j^2$ and aerodynamic torque $k_m u_j^2$. The model of resultant thrust \mathbf{T}_b and torque \mathbf{M}_b are as follows:

$$\mathbf{T}_b = \sum_{j=1}^K \mathbf{e}_3 F_j^b = \sum_{j=1}^K c_t u_j^2 \mathbf{e}_3 \quad (5)$$

$$\mathbf{M}_b = \sum_{j=1}^K (\mathbf{p}_{r_j}^b \times \mathbf{e}_3 F_j^b + (-1)^{j-1} k_m \mathbf{e}_3 u_j^2)$$

where u_j is the j -th ($1 \leq j \leq K$) rotor's angular speed, c_t is the rotor aerodynamic thrust coefficient, and k_m is the rotor aerodynamic torque coefficient. $\mathbf{p}_{r_j}^b$ is the j -th rotor's position in the body frame.

As shown in Fig. 3, according to (5), the typical quadrotor's thrust and torque model is as follows:

$$\mathbf{g}(\mathbf{u}) = \begin{bmatrix} 0 & 0 & 0 & 0 \\ 0 & 0 & 0 & 0 \\ c_t & c_t & c_t & c_t \\ -c_t l_y & c_t l_y & c_t l_y & -c_t l_y \\ -c_t l_x & -c_t l_x & c_t l_x & c_t l_x \\ k_m & -k_m & k_m & -k_m \end{bmatrix} \begin{bmatrix} u_1^2 \\ u_2^2 \\ u_3^2 \\ u_4^2 \end{bmatrix} \quad (6)$$

where l_x and l_y are the length and width of every arm of the quadrotor.

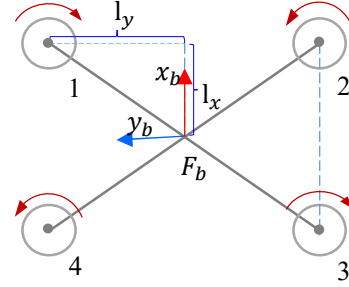


Fig. 3. The structure of the quadrotor.

To determine the covariance matrix of dynamic factor, an explicit noise model with additive Gaussian white noise is assumed as follows:

$$F_j = c_t u_j^2 + n_A, n_A \sim \mathcal{N}(0, s) \quad (7)$$

where s is the variance. Based on the noise model assumption, the thrust covariance matrix \mathbf{P}_T^i and torque covariance matrix \mathbf{P}_M^i of the quadrotor can be derived as follows:

$$\begin{aligned} \mathbf{P}_T^i &= 4 \begin{bmatrix} 0 & 0 & 0 \\ 0 & 0 & 0 \\ 0 & 0 & s \end{bmatrix} \\ \mathbf{P}_M^i &= 4 \begin{bmatrix} l_y^2 s & 0 & 0 \\ 0 & l_x^2 s & 0 \\ 0 & 0 & k_m^2 s \end{bmatrix} \end{aligned} \quad (8)$$

Moreover, the dynamic model (1) ignores the actuator's constraints due to its driving capability. For example, there is a time-constant t_c in the motor, so the whole motor dynamic is assumed to behave as a first-order system [48]. Therefore, the actual actuator's model is as follows:

$$\dot{\mathbf{u}} = \frac{\mathbf{u}_{cmd} - \mathbf{u}}{t_c} \quad (9)$$

where \mathbf{u}_{cmd} is the control command.

B. Positioning based on FGO

For simplicity, we assume that the observations of the absolute factor include position, attitude, velocity, and angular velocity in the simulation. We use multivariate Gaussian measurement assumption for state observation [36]:

$$\Phi_{\mathbf{x}} \propto \exp\left\{-\frac{1}{2} \|\mathbf{z}(\mathbf{x}_c) - \mathbf{z}_c\|_{\mathbf{P}_c}^2\right\} \quad (10)$$

where \mathbf{z}_c is the actual observation, and $\mathbf{z}(\mathbf{x}_c)$ is the predicted observation model.

In addition, the relative pose transformation \mathbf{T}_{l+1}^l from the timestamp l to the timestamp $l+1$ is denoted as follows:

$$\mathbf{T}_{l+1}^l = (\mathbf{T}_{b_l}^w)^{-1} \mathbf{T}_{b_{l+1}}^w \quad (11)$$

where $\mathbf{T}_{b_l}^w$ represents the UAV's pose at the timestamp l , $\mathbf{T}_{b_{l+1}}^w$ represent the UAV's pose at the timestamp $l+1$.

Hence, the relative factor is simplified as:

$$\Phi_{\mathbf{L}} \propto \exp\left\{-\frac{1}{2} \left\| \text{Logmap} \left\{ \mathbf{T}_{l+1}^l (\mathbf{T}_{b_{l+1}}^w)^T \mathbf{T}_{b_l}^w \right\} \right\|_{\mathbf{P}_l^l}^2 \right\} \quad (12)$$

where \mathbf{P}_l^l is the covariance matrix of a relative pose from timestamp l to timestamp $l+1$.

Based on (10) and (12), the residuals of absolute factor and relative factor are denoted as follows, respectively:

> REPLACE THIS LINE WITH YOUR MANUSCRIPT ID NUMBER (DOUBLE-CLICK HERE TO EDIT) <

$$\begin{aligned} \mathbf{r}_c^A &= z(\mathbf{x}_c) - \mathbf{z}_c \\ \mathbf{r}_l^R &= \text{Logmap} \left\{ \mathbf{T}_{l+1}^l (\mathbf{T}_{b_{l+1}}^w)^T \mathbf{T}_{b_l}^w \right\} \end{aligned} \quad (13)$$

C. MPC based on FGO

The general MPC problem is as follows [10]:

$$\min_{\mathbf{u}_{0:N-1}} \sum_{k=0}^{N-1} (\mathbf{x}_k^T \mathbf{W}_k \mathbf{z}_k^r + \mathbf{u}_k^T \mathbf{Y}_k \mathbf{u}_k^r) + \mathbf{x}_N^T \mathbf{W}_N \mathbf{x}_N^r, \quad (14)$$

$$s. t. \mathbf{x}_{k+1} = F(\mathbf{x}_k, \mathbf{u}_k), 0 \leq k \leq N-1, \mathbf{x}_0 = \mathbf{x}_{init},$$

$$\mathbf{u}_{min} \leq \mathbf{u}_k \leq \mathbf{u}_{max},$$

where $\mathbf{W}_k = \mathbf{H}_k^T \mathbf{H}_k \geq 0$ and $\mathbf{W}_N \geq 0$ are the real symmetric matrices and \mathbf{Y}_k is a symmetric real matrix. \mathbf{u}_k and \mathbf{u}_k^r ($0 \leq k \leq N-1$) are the input vector and the input set-point vector, respectively. \mathbf{z}_k^r ($1 \leq k \leq N-1$) and \mathbf{x}_N^r are reference states.

The objective function of MPC is essentially the sum of the squares of various error terms, including distances and input constraints for a period. The distance error is the discrepancy between the predicted states and the pre-set reference states. The input constraints include the bound limit and rate limit.

We consider \mathbf{u}^r as the initial value when implementing the FGO's iterative solver. The control input's change rate $\mathbf{u}_t - \mathbf{u}_{t+1}$ of actuators is restricted due to its driving capability. Furthermore, the input adheres to the actuator's bound limit function $h(\mathbf{u})$. Further details will be discussed in Section IV. Consequently, (14) can be reformulated for representation in a factor graph as follows:

$$\min_{\mathbf{u}_{0:N-1}} \left\{ \begin{aligned} & \sum_{k=1}^{N-1} \|\mathbf{x}_k - \mathbf{z}_k^r\|_{\mathbf{Q}_k}^2 + \|\mathbf{x}_N - \mathbf{x}_N^r\|_{\mathbf{Q}_N}^2 \\ & + \sum_{t=0}^{N-2} \|\mathbf{u}_t - \mathbf{u}_{t+1}\|_{\mathbf{R}_t}^2 + \sum_{j=0}^{N-1} \|h(\mathbf{u}_j)\|_{\mathbf{Q}_{lim}}^2 \end{aligned} \right\}, \quad (15)$$

$$s. t. \mathbf{x}_{k+1} = F(\mathbf{x}_k, \mathbf{u}_k), 0 \leq k \leq N-1, \mathbf{x}_0 = \mathbf{x}_{init}$$

where \mathbf{Q}_k , \mathbf{Q}_N , \mathbf{R}_t , and \mathbf{Q}_{lim} represent different weighting matrices.

IV. METHODOLOGY

We combine positioning and control into a quadratic problem. Assuming M is the number of states to be estimated and N is the length of the predicted states. The unknown variables are $\boldsymbol{\chi} = \{\mathbf{x}_{-M+1:N}^T, \mathbf{u}_{0:N-1}^T\}^T$. The unified optimization problem combines absolute factors, relative factors, and control-related factors. Therefore, JPCM's optimization problem is as follows:

$$\min_{\boldsymbol{\chi}} \left\{ \begin{aligned} & \sum_{c=-M+1}^0 \|\mathbf{r}_c^A\|_{\mathbf{P}_c^A}^2 + \sum_{l=-M+1}^{-1} \|\mathbf{r}_l^R\|_{\mathbf{P}_l^R}^2 + \sum_{i=0}^{N-1} \|\mathbf{r}_i^D\|_{\mathbf{P}_i^D}^2 \\ & + \sum_{k=1}^N \|\mathbf{r}_k^{ref}\|_{\mathbf{Q}_k}^2 + \sum_{t=0}^{N-2} \|\mathbf{r}_t^U\|_{\mathbf{R}_t}^2 + \sum_{j=0}^{N-1} \|h(\mathbf{u}_j)\|_{\mathbf{Q}_{lim}}^2 \end{aligned} \right\} \quad (16)$$

Additionally, the control part involves the reference trajectory factor residuals $\mathbf{r}^{ref} = \mathbf{x} - \mathbf{x}^{ref}$, dynamic factor residuals $\mathbf{r}_i^D = \mathbf{x}_{i+1} - F(\mathbf{x}_i, \mathbf{u}_i)$, control limit factor residuals $\mathbf{r}_t^U = \mathbf{u}_t - \mathbf{u}_{t+1}$, and input constraint factor residuals $h(\mathbf{u}_j)$. These factors are further explained in the following sections.

To simplify the cost function of (16), we obtain:

$$\min_{\boldsymbol{\chi}} \{f_{subpos} + \|z(\mathbf{x}_0) - \mathbf{z}_0\|_{\mathbf{P}_0}^2 + f_{dyn} + f_{MPC}\} \quad (17)$$

where $f_{dyn} = \sum_{i=0}^{N-1} \|\mathbf{r}_i^D\|_{\mathbf{P}_i^D}^2$ is the dynamic-related cost term, and f_{MPC} is the cost function of MPC. Absolute factors and relative factors are reformulated to express the residuals $z(\mathbf{x}_0) - \mathbf{z}_0$ for the initial state \mathbf{x}_0 and the cost function term f_{subpos} for the subsequent states. If only the current state \mathbf{x}_0 is considered, f_{subpos} is zero.

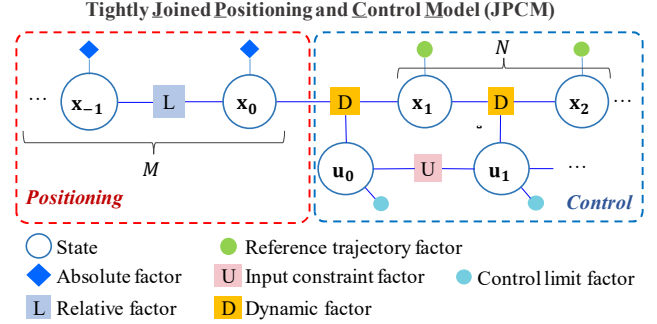


Fig. 4. The factor graph of the proposed tight JPCM. The absolute factor and relative factor are two types of factors generated from common sensors, respectively. The dynamic factor is derived from the UAV's dynamic model, which bridges the gap between positioning and the control module. The reference trajectory factor makes predicted states close to the pre-planned trajectory.

Therefore, we provide a unified factor graph framework to implement the proposed JPCM. As illustrated in Fig. 4 this unified factor graph slides over a time window, which contains M states and N predicted states. The positioning component, highlighted in red, incorporates both absolute and relative factors. In our simulation, $N = 20$, and M depends on the size of the sliding window. For example, if only one state is considered, then $M = 1$.

Additionally, the control component comprises the dynamic factor, reference trajectory factor, input constraint factor, and control limit factor. To bridge the gap between positioning and control, the dynamic factor imposes dynamic constraints on the states at adjacent moments from \mathbf{x}_0 to \mathbf{x}_N . The reference trajectory factor guides the predicted trajectory towards the pre-planned trajectory.

A. Dynamic factor

The dynamic factor serves as a crucial link, bridging the gap between positioning and control. The discrete form of state propagation is $\mathbf{x}_{i+1} = \mathbf{x}_i + \dot{\mathbf{x}}_i \Delta t$. Thus, ignoring aerodynamic drag, the dynamic error can be represented through $\mathbf{r}_i^D = [\mathbf{e}_p^T, \mathbf{e}_\theta^T, \mathbf{e}_v^T, \mathbf{e}_\omega^T]^T = \mathbf{x}_{i+1} - \mathbf{x}_i - \dot{\mathbf{x}}_i \Delta t$ as follows:

$$\begin{aligned} \mathbf{e}_p &= \mathbf{p}_{b_{i+1}}^w - \mathbf{v}_{b_i}^w * \Delta t - \mathbf{p}_{b_i}^w \\ \mathbf{e}_\theta &= \text{Log}(\mathbf{R}_{w_i}^{b_{i+1}} \mathbf{R}_{b_i}^w (\mathbf{I}_{3 \times 3} + \boldsymbol{\omega}_b^* \Delta t)) \\ \mathbf{e}_v &= \mathbf{v}_{b_{i+1}}^w - \mathbf{v}_{b_i}^w - (-\mathbf{R}_G^w \mathbf{e}_3 g + \mathbf{R}_{b_i}^w \mathbf{T}_{b_i} / m_b) \cdot \Delta t \\ \mathbf{e}_\omega &= \boldsymbol{\omega}_{b_{i+1}} - \boldsymbol{\omega}_{b_i} - \mathbf{I}_b^{-1} (\mathbf{M}_{b_i} - \boldsymbol{\omega}_{b_i} \times \mathbf{I}_b \boldsymbol{\omega}_{b_i}) \cdot \Delta t \end{aligned} \quad (18)$$

where Δt is the period between two contiguous states. $\text{Log}(\ast)$ and $\text{Exp}(\ast)$ represent and Logarithmic map and Exponential map of Lie theory, respectively.

To propagate covariance, the dynamic model factor's error function $\mathbf{r}_i^D = [\bar{\mathbf{e}}_p^T, \bar{\mathbf{e}}_\theta^T, \bar{\mathbf{e}}_v^T, \bar{\mathbf{e}}_\omega^T]^T$ can be derived from the error model (18):

> REPLACE THIS LINE WITH YOUR MANUSCRIPT ID NUMBER (DOUBLE-CLICK HERE TO EDIT) <

$$\begin{aligned}
\bar{\mathbf{e}}_p &= \mathbf{R}_w^{b_i} m_b (\mathbf{p}_{b_{i+1}}^w - \mathbf{v}_{b_i}^w \Delta t + 0.5 \mathbf{R}_G^w \mathbf{e}_3 g \Delta t^2 - \mathbf{p}_{b_i}^w) \\
&\quad - 0.5 \mathbf{T}_{b_i} \Delta t^2 \\
\bar{\mathbf{e}}_\theta &= \text{Log}(\mathbf{R}_w^{b_i} \mathbf{R}_{b_{i+1}}^w) - \boldsymbol{\omega}_{b_i} \Delta t \\
\bar{\mathbf{e}}_v &= \mathbf{R}_w^{b_i} m_b (\mathbf{v}_{b_{i+1}}^w - \mathbf{v}_{b_i}^w + \mathbf{R}_G^w \mathbf{e}_3 g \Delta t) - \mathbf{T}_{b_i} \Delta t \\
\bar{\boldsymbol{\omega}} &= \mathbf{I}_b (\boldsymbol{\omega}_{b_{i+1}} - \boldsymbol{\omega}_{b_i}) - (\mathbf{M}_{b_i} - \boldsymbol{\omega}_{b_i} \times \mathbf{I}_b \boldsymbol{\omega}_{b_i}) \cdot \Delta t
\end{aligned} \tag{19a}$$

If aerodynamic drag is further considered, according to (2), the velocity component $\bar{\mathbf{e}}_v$ of the dynamic factor's residual is as follows:

$$\bar{\mathbf{e}}_v = \mathbf{R}_w^{b_i} m_b (\mathbf{v}_{b_{i+1}}^w - \mathbf{v}_{b_i}^w + \mathbf{R}_G^w \mathbf{e}_3 g \Delta t) - \mathbf{T}_{b_i} \Delta t - \mathbf{D} \mathbf{R}_w^{b_i} \mathbf{v}_{b_i}^w \Delta t \tag{19b}$$

According to (8) and (19), the covariance matrix of $\bar{\mathbf{e}}_v$ and $\bar{\boldsymbol{\omega}}$ are $\mathbf{P}_T^i \Delta t^2$ and $\mathbf{P}_M^i \Delta t^2$, respectively. Moreover, the covariance matrix of $\bar{\mathbf{e}}_p$ is set by $0.25 \mathbf{P}_T^i \Delta t^4$. The Jacobian matrix is provided in the Appendix.

B. Control limit factor

The control limit factor is designed to ensure that the control input meets the actuator's limits. Defining the hinge loss cost function $\mathbf{E} = h(\mathbf{u}_j)$ for the control input inequality, which is as follows:

$$\mathbf{E}_i = \begin{cases} u_{min}^j + u_{thr}^j - \mathbf{u}_j(i) & \text{if } \mathbf{u}_j(i) < u_{min}^j + u_{thr}^j \\ \mathbf{u}_j(i) - u_{max}^j + u_{thr}^j & \text{if } u_{max}^j - u_{thr}^j \leq \mathbf{u}_j(i) \\ 0 & \text{otherwise} \end{cases} \tag{20}$$

($1 \leq i \leq K$)

where u_{min}^j is the input lower bound, and u_{max}^j is the input upper bound, and u_{thr}^j is the threshold value. The values of bounds and threshold are illustrated in Table II. In addition, \mathbf{Q}_{lim} is a control limit factor's weighting matrix which determines how fast the error grows as the value approaches the limit.

B. Reference trajectory factor

The reference trajectory factor's residual is as follows:

$$\mathbf{r}^{ref} = (\mathbf{p}, \mathbf{R}, \mathbf{v}) \ominus (\mathbf{p}^r, \mathbf{R}^r, \mathbf{v}^r) \tag{21}$$

where \ominus is a subtraction operator, which calculates the residuals of position, velocity, and rotation. The position residual is $\mathbf{e}_p^{ref} = \mathbf{p} - \mathbf{p}^r$, the velocity residual is $\mathbf{e}_v^{ref} = \mathbf{v} - \mathbf{v}^r$, and the rotation residual is $\mathbf{e}_\theta^{ref} = \text{Log}(\mathbf{R}^T \mathbf{R}^r)$. Then, $\mathbf{r}^{ref} = [(\mathbf{e}_p^{ref})^T (\mathbf{e}_v^{ref})^T (\mathbf{e}_\theta^{ref})^T]^T$. In addition, the reference trajectory factor's covariance \mathbf{Q}_k ($1 \leq k \leq N$) can be configured by users.

V. NUMERICAL EXPERIMENTS

The quadrotor's trajectory control simulation is conducted to evaluate the proposed JPCM's performance. The reference path is assumed a circle. Then, the trajectory is generated by the minimum snap trajectory generation method [49]. Moreover, the Gaussian white noise is added to the thrust and torque of the quadrotor simulator. In particular, the reasons that the simulated dataset is employed to validate the effectiveness of the proposed method lie in three folds: (1) By employing the simulation, the noise of the positioning module can be ideally simulated using the Gaussian noise which is hard to achieve in real environments. (2) The external disturbance can be accurately modeled using the simulated environments which is important for the validation of the proposed method. (3) By using the simulated environments,

the dynamic parameters of the UAV system can also be accurately modeled. More importantly, the full implementation of the model in this paper is open-source to benefit the research community.

The gravity of the quadrotor is 10 N (Newton). The thrust noise's sigma is 0.1N, and the angular speed process noise's sigma is 0.02rad/s. The simulated circle trajectory's linear speed is 5m/s, and its radius is 1.5m. The control frequency is 100 Hz. We assume that the absolute factor's measurement not only includes position, velocity, and angular speed but also the attitude with simulated uncertainty. The proposed unified factor graph is solved using based on the open-source software GTSAM.

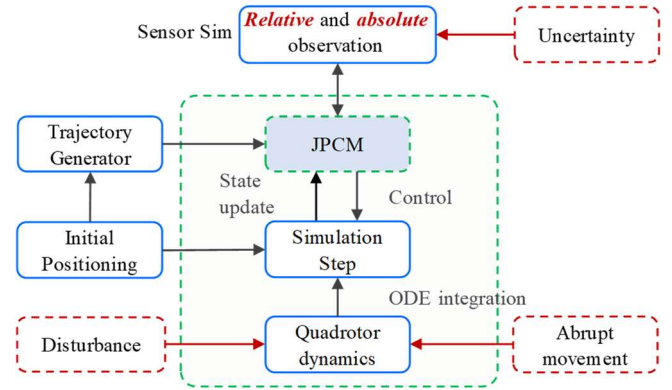


Fig. 5. Simulation framework.

As shown in Fig 5, we simulated a quadrotor based on the quadratic thrust model (5). In our dynamic model, we incorporate various disturbances including the aerodynamic drag, the actuator's time constant, and Gaussian noise. In addition, the performance of the proposed method involving abrupt motion is simulated and studied. This allows us to assess the algorithm's resilience and adaptability under sudden changes in motion dynamics. Moreover, we introduce Gaussian noise into the observation of sensors to simulate large-state uncertainty. This enables us to validate the trajectory tracking performance of our proposed algorithm under challenging conditions characterized by high uncertainty.

A. Performance comparison between MPC and JPCM with high positioning uncertainty

Illustration of the abbreviations of different methods to be evaluated in this paper:

MPC-pre [50] represents the nominal MPC method with highly precise positioning.

MPC [50] represents the nominal MPC method with highly uncertain observation with parameters listed in Table II

JCPM represents the proposed tightly joined positioning and control model with highly uncertain observation for Case 1.

JCPM-SW represents the proposed tightly joined positioning and control model based on a sliding window with highly uncertain observation for Case 2.

Case 1: First, it is assumed that only absolute measurements exist at the current moment. Similarly, a state with uncertainty output by the common positioning module is provided to the MPC and JPCM. Both MPC and JPCM are implemented

> REPLACE THIS LINE WITH YOUR MANUSCRIPT ID NUMBER (DOUBLE-CLICK HERE TO EDIT) <

based on FGO. MPC directly adopts the observation of the current state as the initial state.

Case 2: In addition to the conditions of case 1, it is assumed that the UAV is equipped with a LiDAR and can measure the pose transformation at adjacent timestamps. The length of the variables to be estimated is set to 10. The extrinsic parameter between the LiDAR frame and the body frame is an identity matrix. Verify the feasibility of the proposed method under these conditions. We define JPCM based on sliding window as JPCM-Sliding Window (JPCM-SW). We simulate the relative pose transformation \mathbf{T}_{l+1}^l with the Gaussian white noise \mathbf{n}_l as follows:

$$\mathbf{T}_{l+1}^l = \hat{\mathbf{T}}_{l+1}^l \text{Expmap}(\mathbf{n}_l) \quad (22)$$

where $\hat{\mathbf{T}}_{l+1}^l$ is the true value of relative pose.

All simulation parameters are listed in Table II.

TABLE II
Simulation parameters

Parameters	Case 1	Case 2
M (the length of historical states constrained by observation)	1	10
N (the length of predicted states in control)	20	
Position sigma	0.20 m	
Rotation sigma	0.03 rad	
Velocity sigma	0.05 m/s	
Angular velocity sigma	0.001 rad/s	
Sigma of \mathbf{T}_{l+1}^l	$\text{diag}\{0.03^2\mathbf{I}_3^T, 0.03^2\mathbf{I}_3^T\}$	
\mathbf{P}_l^l	$\text{diag}\{0.03^2\mathbf{I}_3^T, 0.03^2\mathbf{I}_3^T\}$	
\mathbf{Q}_k	$\text{diag}\{0.03^2\mathbf{I}_3^T, 0.3^2\mathbf{I}_3^T, 3^2\mathbf{I}_3^T\}$	
\mathbf{Q}_N	$\text{diag}\{0.01^2\mathbf{I}_3^T, 0.3^2\mathbf{I}_3^T, 3^2\mathbf{I}_3^T\}$	
\mathbf{R}_t	$\text{diag}\{1000\mathbf{I}_4^T\}$	
u_{min}	12000	
u_{thr}	100	
u_{max}	18000	

1) Simulation Results of Case 1

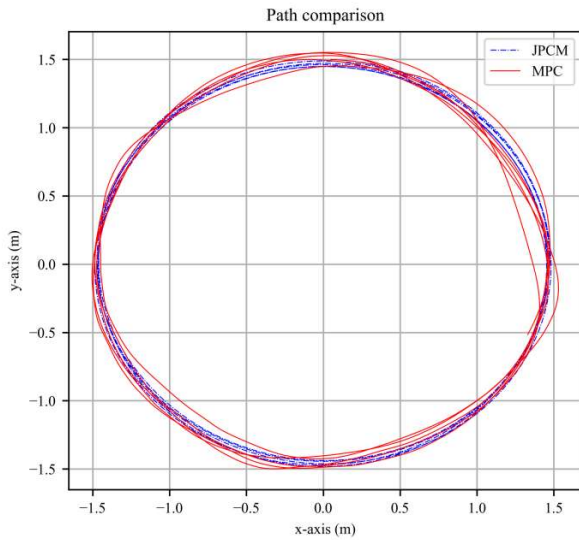


Fig. 7. Case 1: The paths of MPC and JPCM (linear speed = 5m/s, radius = 1.5m). The red solid line and blue solid line represent the tracking path based on MPC and the tracking path based on JPCM, respectively.

For case 1, Fig 7 illustrates the path of MPC and JPCM, which shows that JPCM aligns more closely with the reference path than the MPC method. In contrast, the nominal MPC exhibits significant fluctuation. Furthermore, the rotation and position control errors are depicted in Fig 8. The root mean square errors (RMSEs) are also summarized in Table I. MPC-pre represents the MPC method with high-precision positioning. When positioning measurements are precise, the MPC problem solved by FGO converges to the reference trajectory with minimal control errors. However, compared to JPCM, the control errors of the nominal MPC increase significantly in the presence of large positioning uncertainty. This indicates that noisy positioning adversely affects the control performance of UAVs. Moreover, Table I reveals that both the position and rotation control errors of the proposed JPCM are reduced compared to the nominal MPC with large noise positioning.

TABLE III

THE TRAJECTORY FOLLOWING RMSE OF MPC-PRE (MPC WITH PRECISE POSITIONING), MPC, JPCM, AND JPCM-SW (SLIDING WINDOW-BASED JPCM)

Method	Position RMSE (m)			Rotation RMSE (rad)		
MPC-pre	0.010	0.010	0.005	0.005	0.005	0.004
MPC	0.068	0.066	0.055	0.246	0.151	0.251
JPCM	0.031	0.019	0.015	0.031	0.018	0.158
JPCM-SW	0.017	0.017	0.019	0.010	0.011	0.205

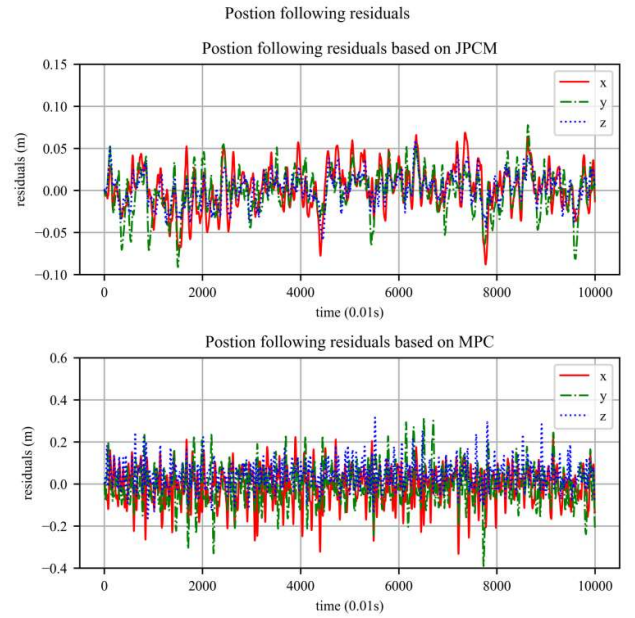


Fig. 8. Case 1: Position following residuals comparison: JPCM and MPC.

As shown in Fig 9, under highly uncertain observations, the MPC's control inputs often reach the upper or lower bound. On the contrary, the control inputs of the JPCM are relatively concentrated. The MPC is probing at the edge of the control boundary, indicating that the solution of the control quantity is on the verge of reaching a critical constraint. Specifically, when the positioning value strays excessively from the intended target, the optimization process may fail to procure a viable solution.

> REPLACE THIS LINE WITH YOUR MANUSCRIPT ID NUMBER (DOUBLE-CLICK HERE TO EDIT) <

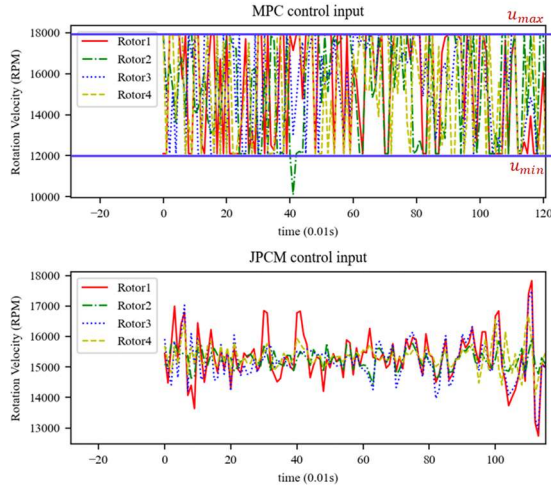


Fig. 9. Case 1: The comparison of control input between MPC and JPCM. Most control inputs are strictly limited between upper and lower bounds.

2) Simulation Results of Case 2

As for case 2, the JPCM-SW is conducted with $M = 10$. As demonstrated in Table III, the JPCM-SW method exhibits a slight reduction in both the x-axis and y-axis position following residuals when compared to the standard JPCM method. The enhanced performance of JPCM-SW is achieved through a tightly integrated approach that effectively combines historical observations with control objectives. By utilizing more historical information, the JPCM-SW method achieves higher precise control than MPC.

MPC can handle most control tasks effectively when the positioning accuracy is high. However, in urban scenarios where severe positioning noise is prevalent, the trajectory following the error of MPC may be significantly exacerbated. In contrast, the proposed JPCM substantially improves trajectory tracking performance in situations where positioning uncertainty is high. To conclude, the performance of JPCM based on FGO surpasses that of the standard MPC, particularly when precise positioning is not available.

B. Performance comparison under disturbances

(1) Abrupt movements

Sudden winds or brief malfunctions can cause UAVs to experience instantaneous movement. This poses a risk to the stability of the control. The controller should have the ability to maintain a stable status. We refer to the process of recovering to a predetermined trajectory after a rapid and large movement as a “recovery process”. We simulate a rapid and large movement at one moment and investigate the “recovery process”.

As illustrated in Fig 10, an unplanned movement $\Delta \mathbf{p}_b^w = [0.00\text{m}, 0.30\text{m}, -0.40\text{m}]^T$ is simulated at 0.5 seconds, and the UAV controlled by JPCM returns to the planned trajectory in about three seconds. In comparison to MPC, the recovery process of the proposed JPCM method takes a longer duration. However, JPCM renders a smoother position tracking error curve according to Fig. 10. The disadvantage is that when JPCM experiences significant movement disturbances, the control delay will be greater. Conversely, in scenarios that

pursue smoother control, this becomes an advantage. For example, in the case of positioning outliers or spoofing, smoother and slower JPCM is more robust than MPC. Besides, the control delay can be accepted in practical systems.

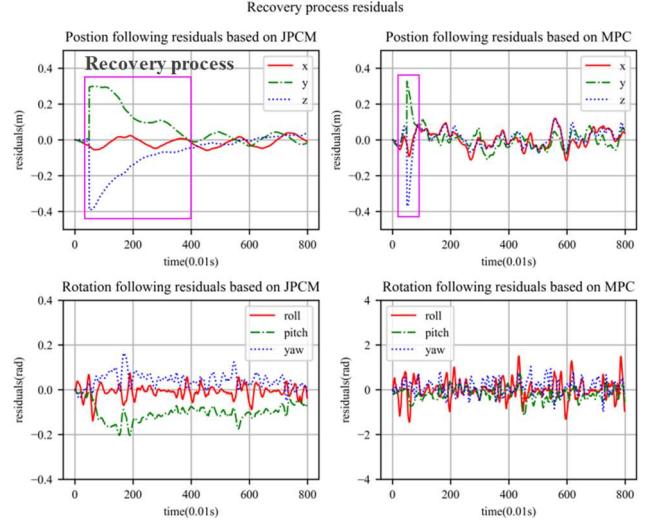


Fig. 10. Position and rotation following residuals after abrupt movement.

(2) Aerodynamic drag force

First, we investigate the performance of JPCM affected by the aerodynamic drag (not considering aerodynamic drag factors in the controller). Then, to mitigate the effects of aerodynamic drag force, we introduce a drag-aiding JPCM method, namely **JPCM-Drag**.

To evaluate the performance of the proposed JPCM under the simulated parameters in Table II Case 1, four prevalent aerodynamic drag coefficients are strategically chosen. An analysis of the data presented in Table IV indicates a direct correlation between the trajectory position tracking error of JPCM and the magnitude of the aerodynamic drag coefficient. Despite the increase in error, it is noteworthy that the system maintains its stability and does not diverge.

TABLE IV
THE TRAJECTORY FOLLOWING RMSE OF JPCM AND JPCM-DRAG WITH AERODYNAMIC DRAG FORCE

Method	Drag parameter	Position RMSE (m)			Rotation RMSE (rad)		
JPCM	0	0.026	0.025	0.018	0.022	0.016	0.024
JPCM	$0.1\mathbf{I}_{3 \times 3}$	0.040	0.031	0.024	0.023	0.013	0.045
JPCM	$0.2\mathbf{I}_{3 \times 3}$	0.053	0.047	0.035	0.018	0.023	0.040
JPCM	$0.3\mathbf{I}_{3 \times 3}$	0.067	0.061	0.039	0.032	0.036	0.062
JPCM- Drag	$0.3\mathbf{I}_{3 \times 3}$	0.031	0.025	0.028	0.011	0.037	0.064

Eliminating aerodynamic drag effects: JPCM-Drag incorporates the aerodynamic drag into the error function (19b) and recalculates the Jacobian matrix of the modified dynamic model factor. This is achieved by integrating a non-zero coefficient matrix, denoted as \mathbf{D} , into the formulas provided in the Appendix. A specific instance of this method is demonstrated where \mathbf{D} is set to $0.3\mathbf{I}_{3 \times 3}$ that is consistent with the actual system level. As shown in Fig 11, the JPCM method reveals a significant deviation in the circular trajectory towards the center of the circle. The shift is attributed to the

influence of aerodynamic drag. The JPCM-Drag method, which accounts for this drag effect, shows a tendency to converge towards the pre-set trajectory. Furthermore, when the JPCM-Drag method is implemented, the RMSE of the position following closely approximates the RMSE in scenarios devoid of aerodynamic drag. This observation underscores the efficacy of the JPCM-Drag method in neutralizing the impact of aerodynamic drag.

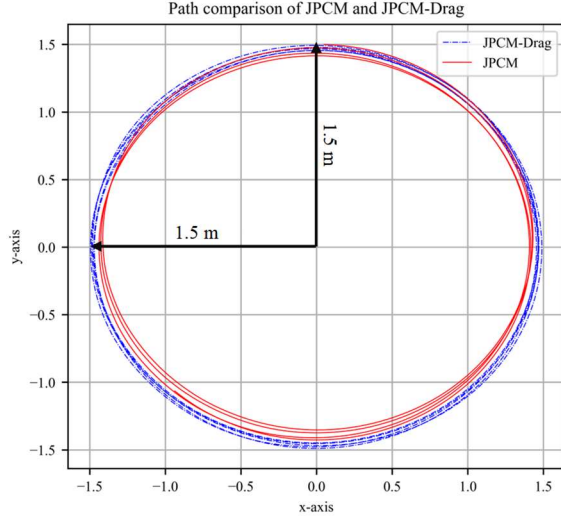


Fig. 11. Path comparison of JPCM method and JPCM-Drag method with aerodynamic drag ($\mathbf{D} = 0.3\mathbf{I}_{3 \times 3}$).

(2) Actuator Time constant

TABLE V

THE TRAJECTORY FOLLOWING RMSE OF JPCM WITH ACTUATOR TIME CONSTANT

t_c	Position RMSE (m)			Rotation RMSE (rad)		
10ms	0.031	0.019	0.015	0.031	0.007	0.158
25ms	0.026	0.017	0.017	0.010	0.010	0.014
50ms	0.027	0.017	0.023	0.028	0.022	0.035
60ms	divergence					
100ms	divergence					

The whole actuator's dynamic is approximately a first-order system [48], in which a time constant is a key factor affecting system convergence. The stability is tested by simulating different actuators at constant time.

An examination of Table V reveals a key characteristic of the system's performance: when the time constant remains at or below 50ms, the controller error does not exhibit a significant increase. Despite the impacts imposed by the actuator time constant, the system can consistently and reliably accomplish the control task. This observation underscores the system's robustness and its ability to maintain stability under these specific conditions. Nevertheless, as the time constant progressively escalates to a certain threshold, the controller begins to diverge. In actual UAV applications, the time constant can be obtained by analyzing the response time of the actuator.

VI. DISCUSSION

When substantial errors occur in the initial state, they can induce significant fluctuations in the predicted trajectory, as evidenced by the MPC in Fig 12. This discrepancy arises

because the navigation solution fails to align with the actual position of the UAV, potentially leading to unstable control. Furthermore, the UAV model is characterized by high nonlinearity, and any attitude jitter can pose a significant safety risk. This is due to the potential for rapid, unpredictable changes in the UAV's orientation, which could lead to loss of control or collision.

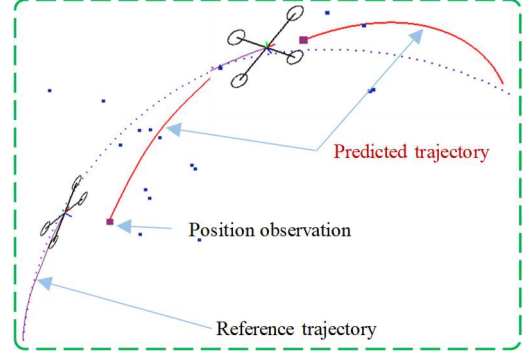


Fig. 12. State uncertainty has an impact on the stability of control.

However, a control mechanism that incorporates the initial positioning probability may mitigate the risks due to positioning uncertainty. This is primarily because the probabilistic representation of positioning can minimize the control overshoot, which is a common issue in dynamic control systems.

Only considering the current state \mathbf{x}_0 , the cost function in JPCM is equivalent to:

$$f_{JPCM} = f_{MPC} + f_{dyn} + \|\mathbf{H}_0 \mathbf{x}_0 - \mathbf{z}_{ob}\|_{\mathbf{P}_0}^2 \quad (23)$$

where \mathbf{H}_0 is the Jacobian matrix at $\hat{\mathbf{x}}_0$, and \mathbf{z}_{ob} is the observation of the initial state.

MPC can handle control problems when the positioning accuracy is high. In other words, if the covariance matrix \mathbf{P}_0 in (23) approaches $\mathbf{0}$, that is, when the positioning accuracy is high, JPCM equivalents the MPC problem. However, in real-world applications that permeate our daily lives, such as autonomous vehicles navigating city streets and cooperative robots performing tasks in indoor environments, the financial burden associated with achieving high-precision capabilities may be substantial. In some instances, the attainment of such precision may not even be feasible, thus posing significant challenges to the implementation of these advanced technologies. In contrast, JPCM is equivalent to relaxing the fixed-value constraints in the MPC problem into a probabilistic constraint on the initial variables. This relaxation allows for greater flexibility in the control mechanism, potentially improving the UAV's ability to handle unexpected changes in its environment or initial state.

Moreover, the recovery process demonstrates that the proposed JPCM necessitates a longer duration to revert to the pre-set path in comparison to the conventional MPC. This can be attributed to the simultaneous optimization of positioning and control. The constraints imposed by the planned trajectory exert a pull on the estimated state, drawing it closer to the trajectory, which, in turn, diminishes the control energy. The traditional MPC, with its ability to plan actions with decisiveness, is more prone to fluctuations with bad positioning. It is a stark contrast to the controller based on

JPCM, which exhibits resilience to faults triggered by irregular positioning or sudden, large-scale movements. Should users seek to enhance the response speed, they have the option to strategically decrease the value of \mathbf{P}_0 .

VII. CONCLUSION AND FUTURE WORK

To establish a tightly integrated model with positioning and control, we propose a tight JPCM. The model combines positioning and control into a unified factor graph. Additionally, we provide a design framework for the unified factor graph, formulating a series of factors pertinent to positioning, dynamic control and trajectory tracking. These factors are instrumental in ensuring precise and efficient control over the system's trajectory. Finally, a quadrotor simulator is used to evaluate the proposed method's performance. The simulation results show that the proposed method is convergent with smaller errors than the conventional MPC. In simulation, the proposed method is tested with three kinds of disturbances. For future research, we will conduct real-world experiments. In addition, the design law governing the control weight matrix of the FGO needs to be explained further.

VIII. ACKNOWLEDGMENT

This paper is funded by the MEITUAN ACADEMY OF ROBOTICS SHENZHEN under the project "Vision Aided GNSS-RTK Positioning for UAV System in Urban Canyons (ZGHQ)". This paper is also funded by the PolyU Research Institute for Advanced Manufacturing (RIAM) under the project "Unmanned Aerial Vehicle Aided High Accuracy Additive Manufacturing for Carbon Fiber Reinforced Thermoplastic Composites Material (CD8S)".

IX. APPENDIX

Jacobian matrix of dynamic factor

The Jacobian matrix of error \mathbf{e}^D to state \mathbf{x}_i is as follows:

$$J_{\mathbf{x}_i}^D = \begin{bmatrix} -\mathbf{R}_w^{b_i} m_b & (\mathbf{R}_w^{b_i} \mathbf{p}_p)^\times & -\mathbf{R}_w^{b_i} m_b \Delta t & \mathbf{0} \\ \mathbf{0} & -\mathbf{R}_w^{b_{i+1}} \mathbf{R}_w^{b_i} & \mathbf{0} & -\mathbf{I}_{3 \times 3} \Delta t \\ \mathbf{0} & \frac{\partial \bar{\mathbf{e}}_v}{\partial \mathbf{R}_w^{b_i}} & \frac{\partial \bar{\mathbf{e}}_v}{\partial \mathbf{v}_{b_i}^w} & \mathbf{0} \\ \mathbf{0} & \mathbf{0} & \mathbf{0} & \frac{\partial \bar{\mathbf{e}}_\omega}{\partial \boldsymbol{\omega}_{b_i}} \end{bmatrix} \quad (24)$$

where \mathbf{p}_p , \mathbf{p}_v , $\frac{\partial \bar{\mathbf{e}}_v}{\partial \mathbf{R}_w^{b_i}}$, $\frac{\partial \bar{\mathbf{e}}_v}{\partial \mathbf{v}_{b_i}^w}$, and $\frac{\partial \bar{\mathbf{e}}_\omega}{\partial \boldsymbol{\omega}_{b_i}}$ are as follows:

$$\mathbf{p}_p = m_b (\mathbf{p}_{b_{i+1}}^w - \mathbf{v}_{b_i}^w \Delta t + 0.5 \mathbf{R}_G^w \mathbf{e}_3 g \Delta t^2 - \mathbf{p}_{b_i}^w) \quad (25a)$$

$$\mathbf{p}_v = m_b (\mathbf{v}_{b_{i+1}}^w - \mathbf{v}_{b_i}^w + \mathbf{R}_G^w \mathbf{e}_3 g \Delta t) \quad (25b)$$

$$\frac{\partial \bar{\mathbf{e}}_v}{\partial \mathbf{R}_w^{b_i}} = (\mathbf{R}_w^{b_i} \mathbf{p}_v)^\times - \mathbf{D}(\mathbf{R}_w^{b_i} \mathbf{v}_{b_i}^w)^\times \Delta t \quad (25c)$$

$$\frac{\partial \bar{\mathbf{e}}_v}{\partial \mathbf{v}_{b_i}^w} \& = -\mathbf{R}_w^{b_i} m_b - \mathbf{D} \mathbf{R}_w^{b_i} \Delta t \quad (25d)$$

$$\frac{\partial \bar{\mathbf{e}}_\omega}{\partial \boldsymbol{\omega}_{b_i}} = \begin{bmatrix} -\mathbf{I}_b^1 & (\mathbf{I}_b^3 - \mathbf{I}_b^2) \omega_3 & (\mathbf{I}_b^3 - \mathbf{I}_b^2) \omega_2 \\ (\mathbf{I}_b^1 - \mathbf{I}_b^3) \omega_3 & -\mathbf{I}_b^2 & (\mathbf{I}_b^1 - \mathbf{I}_b^3) \omega_1 \\ (\mathbf{I}_b^2 - \mathbf{I}_b^1) \omega_2 & (\mathbf{I}_b^2 - \mathbf{I}_b^1) \omega_1 & -\mathbf{I}_b^3 \end{bmatrix} \Delta t \quad (25e)$$

The Jacobian matrix of error \mathbf{e}^D to state \mathbf{x}_{i+1} is as follows:

$$J_{\mathbf{x}_{i+1}}^D = \begin{bmatrix} \mathbf{R}_w^{b_i} m_b & \mathbf{0} & \mathbf{0} & \mathbf{0} \\ \mathbf{0} & \mathbf{I}_{3 \times 3} & \mathbf{0} & \mathbf{0} \\ \mathbf{0} & \mathbf{0} & \mathbf{R}_w^{b_i} m_b & \mathbf{0} \\ \mathbf{0} & \mathbf{0} & \mathbf{0} & \mathbf{I}_b \end{bmatrix} \quad (26)$$

The Jacobian matrix of error $\bar{\mathbf{e}}_v$ to control input \mathbf{u} is as follows:

$$J_{\mathbf{u}}^{\bar{\mathbf{e}}_v} = J_{\mathbf{T}}^{\bar{\mathbf{e}}_v} J_{\mathbf{u}}^{\mathbf{T}} = -\Delta t \begin{bmatrix} \mathbf{0}_4^T \\ \mathbf{0}_4^T \\ 2c_t \mathbf{u}^T \end{bmatrix} \quad (27)$$

The Jacobian matrix of error $\bar{\mathbf{e}}_\omega$ to control input \mathbf{u} is as follows:

$$J_{\mathbf{M}}^{\bar{\mathbf{e}}_\omega} = J_{\mathbf{M}}^{\bar{\mathbf{e}}_\omega} J_{\mathbf{u}}^{\mathbf{M}} = -2c_t \Delta t \left\{ \begin{bmatrix} \mathbf{p}_{r_1}^b \times \mathbf{e}_3 & \cdots & \mathbf{p}_{r_k}^b \times \mathbf{e}_3 \\ +[\mathbf{k}_m \mathbf{e}_3 & \cdots & (-1)^k \mathbf{k}_m \mathbf{e}_3] \end{bmatrix} \begin{bmatrix} \mathbf{u}^T \\ \mathbf{u}^T \\ \mathbf{u}^T \end{bmatrix} \right\} \quad (28)$$

REFERENCES

- [1] D. Yin, X. Yang, H. Yu, S. Chen, and C. Wang, "An air-to-ground relay communication planning method for UAVs swarm applications," *IEEE Transactions on Intelligent Vehicles*, 2023.
- [2] Y. Liu, C. Yang, X. Chen, and F. Wu, "Joint Hybrid Caching and Replacement Scheme for UAV-Assisted Vehicular Edge Computing Networks," *IEEE Transactions on Intelligent Vehicles*, 2023.
- [3] M. Eskandari, H. Huang, A. V. Savkin, and W. Ni, "Model predictive control-based 3D navigation of a RIS-equipped UAV for LoS wireless communication with a ground intelligent vehicle," *IEEE Transactions on Intelligent Vehicles*, 2022.
- [4] M. Samir, C. Assi, S. Sharafeddine, D. Ebrahimi, and A. Ghayeb, "Age of information aware trajectory planning of UAVs in intelligent transportation systems: A deep learning approach," *Ieee T Veh Technol*, vol. 69, no. 11, pp. 12382-12395, 2020.
- [5] M. Adil, H. Song, S. Mastorakis, H. Abulkasim, A. Farouk, and Z. Jin, "UAV-Assisted IoT Applications, Cybersecurity Threats, AI-Enabled Solutions, Open Challenges With Future Research Directions," *IEEE Transactions on Intelligent Vehicles*, pp. 1-21, 2024, doi: 10.1109/tiv.2023.3309548.
- [6] A. Ryan, M. Zennaro, A. Howell, R. Sengupta, and J. K. Hedrick, "An overview of emerging results in cooperative UAV control," in *2004 43rd IEEE Conference on Decision and Control (CDC)(IEEE Cat. No. 04CH37601)*, 2004, vol. 1: IEEE, pp. 602-607.
- [7] R. Amin, L. Aijun, and S. Shamshirband, "A review of quadrotor UAV: control methodologies and performance evaluation," *International Journal of Automation and Control*, vol. 10, no. 2, pp. 87-103, 2016.
- [8] P. D. Groves, "Principles of GNSS, inertial, and multisensor integrated navigation systems, [Book review]," *IEEE Aerospace and Electronic Systems Magazine*, vol. 30, no. 2, pp. 26-27, 2015.
- [9] X. Liu, W. Wen, and L.-T. Hsu, "Glio: Tightly-coupled gnss/lidar/imu integration for continuous and drift-free state estimation of intelligent vehicles in urban areas," *IEEE Transactions on Intelligent Vehicles*, 2023.

- [10] M. Eskandari, H. Huang, A. V. Savkin, and W. Ni, "Model Predictive Control-Based 3D Navigation of a RIS-Equipped UAV for LoS Wireless Communication With a Ground Intelligent Vehicle," *IEEE Transactions on Intelligent Vehicles*, vol. 8, no. 3, pp. 2371-2384, 2023, doi: 10.1109/tiv.2022.3232890.
- [11] I. A. Mourikis and I. S. Roumeliotis, "A Multi-State Constraint Kalman Filter for Vision-aided Inertial Navigation," presented at the 2007 IEEE International Conference on Robotics and Automation, 2007.
- [12] F. M. Mirzaei and S. I. Roumeliotis, "A Kalman Filter-Based Algorithm for IMU-Camera Calibration: Observability Analysis and Performance Evaluation," *IEEE Transactions on Robotics*, vol. 24, no. 5, pp. 1143-1156, 2008, doi: 10.1109/tro.2008.2004486.
- [13] M. Kaess, H. Johannsson, R. Roberts, V. Ila, J. J. Leonard, and F. Dellaert, "iSAM2: Incremental smoothing and mapping using the Bayes tree," *The International Journal of Robotics Research*, vol. 31, no. 2, pp. 216-235, 2011, doi: 10.1177/0278364911430419.
- [14] W. Wen, T. Pfeifer, X. Bai, and L. T. Hsu, "Factor graph optimization for GNSS/INS integration: A comparison with the extended Kalman filter," *Navigation*, vol. 68, no. 2, pp. 315-331, 2021, doi: 10.1002/navi.421.
- [15] W. Xu, Y. Cai, D. He, J. Lin, and F. Zhang, "FAST-LIO2: Fast Direct LiDAR-Inertial Odometry," *IEEE Transactions on Robotics*, vol. 38, no. 4, pp. 2053-2073, 2022, doi: 10.1109/tro.2022.3141876.
- [16] S. Cao, X. Lu, and S. Shen, "GVINS: Tightly Coupled GNSS-Visual-Inertial Fusion for Smooth and Consistent State Estimation," *IEEE Transactions on Robotics*, vol. 38, no. 4, pp. 2004-2021, 2022, doi: 10.1109/tro.2021.3133730.
- [17] G. He, X. Yuan, Y. Zhuang, and H. Hu, "An Integrated GNSS/LiDAR-SLAM Pose Estimation Framework for Large-Scale Map Building in Partially GNSS-Denied Environments," *IEEE Transactions on Instrumentation and Measurement*, vol. 70, pp. 1-9, 2021, doi: 10.1109/tim.2020.3024405.
- [18] T. Liu, B. Li, C. Guang'e, L. Yang, J. Qiao, and W. Chen, "Tightly Coupled Integration of GNSS/UWB/VIO for Reliable and Seamless Positioning," *IEEE Transactions on Intelligent Transportation Systems*, pp. 1-13, 2023, doi: 10.1109/tits.2023.3314836.
- [19] Y. Zhang, "LILO: A Novel Lidar-IMU SLAM System With Loop Optimization," *IEEE Transactions on Aerospace and Electronic Systems*, vol. 58, no. 4, pp. 2649-2659, 2022, doi: 10.1109/taes.2021.3135234.
- [20] R. Wang, K. Wang, W. Song, and M. Fu, "Aerial-Ground Collaborative Continuous Risk Mapping for Autonomous Driving of Unmanned Ground Vehicle in Off-Road Environments," *IEEE Transactions on Aerospace and Electronic Systems*, vol. 59, no. 6, pp. 9026-9041, 2023, doi: 10.1109/taes.2023.3312627.
- [21] T. Lew, R. Bonalli, and M. Pavone, "Risk-Averse Trajectory Optimization via Sample Average Approximation," *IEEE Robotics and Automation Letters*, pp. 1-8, 2023, doi: 10.1109/lra.2023.3331889.
- [22] X. Ju, D. Xu, and H. Zhao, "Scene-Aware Error Modeling of LiDAR/Visual Odometry for Fusion-Based Vehicle Localization," *IEEE Transactions on Intelligent Transportation Systems*, vol. 23, no. 7, pp. 6480-6494, 2022, doi: 10.1109/tits.2021.3058054.
- [23] W. W. Wen and L.-T. Hsu, "3D LiDAR Aided GNSS NLOS Mitigation in Urban Canyons," *IEEE Transactions on Intelligent Transportation Systems*, vol. 23, no. 10, pp. 18224-18236, 2022, doi: 10.1109/tits.2022.3167710.
- [24] H. F. Ng, G. Zhang, Y. Luo, and L. T. Hsu, "Urban positioning: 3D mapping-aided GNSS using dual-frequency pseudorange measurements from smartphones," *Navigation*, vol. 68, no. 4, pp. 727-749, 2021.
- [25] F. Huang, W. Wen, J. Zhang, C. Wang, and L.-T. Hsu, "Dynamic Object-aware LiDAR Odometry Aided by Joint Weightings Estimation in Urban Areas," *IEEE Transactions on Intelligent Vehicles*, 2023.
- [26] B. Kada and Y. Ghazzawi, "Robust PID controller design for an UAV flight control system," in *Proceedings of the World congress on Engineering and Computer Science*, 2011, vol. 2, no. 1-6, pp. 1-6.
- [27] Y. Zhang, Z. Wu, and T. Wei, "Precise Landing on Moving Platform for Quadrotor UAV via Extended Disturbance Observer," *IEEE Transactions on Intelligent Vehicles*, pp. 1-10, 2024, doi: 10.1109/tiv.2024.3376954.
- [28] Y. Wu, Z. Ding, C. Xu, and F. Gao, "External Forces Resilient Safe Motion Planning for Quadrotor," *IEEE Robotics and Automation Letters*, vol. 6, no. 4, pp. 8506-8513, 2021, doi: 10.1109/lra.2021.3110316.
- [29] Z. Huang and M. Chen, "Augmented Disturbance Observer-Based Appointed-Time Tracking Control of UAVs Under Exogenous Disturbance," *IEEE Transactions on Intelligent Vehicles*, vol. 9, no. 1, pp. 2822-2835, 2024, doi: 10.1109/tiv.2023.3303348.
- [30] S. Sun, A. Romero, P. Foehn, E. Kaufmann, and D. Scaramuzza, "A Comparative Study of Nonlinear MPC and Differential-Flatness-Based Control for Quadrotor Agile Flight," *IEEE Transactions on Robotics*, vol. 38, no. 6, pp. 3357-3373, 2022, doi: 10.1109/tro.2022.3177279.
- [31] W. Wenjie, H. Zhen, C. Rui, J. Feiteng, and S. Huiming, "Trajectory Tracking Control Design for UAV Based on MPC and Active Disturbance Rejection," in *2018 IEEE CSAA Guidance, Navigation and Control Conference (CGNCC)*, 2018: IEEE, pp. 1-5.
- [32] S. S. Mansouri *et al.*, "A unified nmpe scheme for mavs navigation with 3d collision avoidance under position uncertainty," *IEEE Robotics and Automation Letters*, vol. 5, no. 4, pp. 5740-5747, 2020.
- [33] D. Saccani, L. Cecchin, and L. Fagiano, "Multitrajectory model predictive control for safe uav navigation in an unknown environment," *IEEE Transactions on Control Systems Technology*, 2022.

- [34] Z. Liu and L. Cai, "Simultaneous Planning and Execution for Safe Flight of Quadrotors suffering One Rotor Loss and Disturbance," *IEEE Transactions on Aerospace and Electronic Systems*, pp. 1-17, 2023, doi: 10.1109/taes.2023.3265948.
- [35] A. Sharma, G. F. Laupré, and J. Skaloud, "Identifying Aerodynamics of Small Fixed-Wing Drones Using Inertial Measurements for Model-Based Navigation," *NAVIGATION: Journal of the Institute of Navigation*, vol. 70, no. 4, 2023, doi: 10.33012/navi.611.
- [36] S. Yang, G. Chen, Y. Zhang, H. Choset, and F. Dellaert, "Equality Constrained Linear Optimal Control With Factor Graphs," presented at the 2021 IEEE International Conference on Robotics and Automation (ICRA), 2021.
- [37] Q. Zhang, A. Taghvaei, and Y. Chen, "An optimal control approach to particle filtering," *Automatica*, vol. 151, 2023, doi: 10.1016/j.automatica.2023.110894.
- [38] B. Bazzana, T. Guadagnino, and G. Grisetti, "Handling Constrained Optimization in Factor Graphs for Autonomous Navigation," *IEEE Robotics and Automation Letters*, vol. 8, no. 1, pp. 432-439, 2023, doi: 10.1109/ra.2022.3228175.
- [39] M. Xie, A. Escontrela, and F. Dellaert, "A Factor-Graph Approach for Optimization Problems with Dynamics Constraints," p. arXiv:2011.06194doi: 10.48550/arXiv.2011.06194.
- [40] J.-L. Blanco-Claraco, A. Lanza, and G. Reina, "A general framework for modeling and dynamic simulation of multibody systems using factor graphs," *Nonlinear Dynamics*, vol. 105, no. 3, pp. 2031-2053, 2021, doi: 10.1007/s11071-021-06731-6.
- [41] M. Mukadam, J. Dong, F. Dellaert, and B. Boots, "STEAP: simultaneous trajectory estimation and planning," *Autonomous Robots*, vol. 43, no. 2, pp. 415-434, 2018, doi: 10.1007/s10514-018-9770-1.
- [42] M. King-Smith, P. Tsiotras, and F. Dellaert, "Simultaneous Control and Trajectory Estimation for Collision Avoidance of Autonomous Robotic Spacecraft Systems," presented at the 2022 International Conference on Robotics and Automation (ICRA), 2022.
- [43] X. Bai, W. Wen, and L.-T. Hsu, "Time-Correlated Window-Carrier-Phase-Aided GNSS Positioning Using Factor Graph Optimization for Urban Positioning," *IEEE Transactions on Aerospace and Electronic Systems*, vol. 58, no. 4, pp. 3370-3384, 2022, doi: 10.1109/taes.2022.3149730.
- [44] X. Ye, F. Song, Z. Zhang, and Q. Zeng, "A Review of Small UAV Navigation System Based on Multisource Sensor Fusion," *IEEE Sensors Journal*, vol. 23, no. 17, pp. 18926-18948, 2023, doi: 10.1109/jsen.2023.3292427.
- [45] M. Faessler, A. Franchi, and D. Scaramuzza, "Differential Flatness of Quadrotor Dynamics Subject to Rotor Drag for Accurate Tracking of High-Speed Trajectories," *IEEE Robotics and Automation Letters*, vol. 3, no. 2, pp. 620-626, 2018, doi: 10.1109/ra.2017.2776353.
- [46] S. I. Roumeliotis and J. W. Burdick, "Stochastic cloning: a generalized framework for processing relative state measurements," in *Proceedings 2002 IEEE International Conference on Robotics and Automation (Cat. No.02CH37292)*, 11-15 May 2002 2002, vol. 2, pp. 1788-1795 vol.2, doi: 10.1109/ROBOT.2002.1014801.
- [47] C. Chen, Y. Yang, P. Geneva, W. Lee, and G. Huang, "Visual-Inertial-Aided Online MAV System Identification," presented at the 2022 IEEE/RSJ International Conference on Intelligent Robots and Systems (IROS), 2022.
- [48] C.-C. Peng and C.-Y. Su, "Modeling and Parameter Identification of a Cooling Fan for Online Monitoring," *IEEE Transactions on Instrumentation and Measurement*, vol. 70, pp. 1-14, 2021, doi: 10.1109/tim.2021.3104375.
- [49] D. Mellinger and V. Kumar, "Minimum Snap Trajectory Generation and Control for Quadrotors," presented at the IEEE International Conference on Robotics and Automation, 2011.
- [50] Y. Zhang, F. Jiang, G. Chen, V. Agrawal, A. Rutkowski, and F. Dellaert, "Constraint Manifolds for Robotic Inference and Planning," presented at the 2023 IEEE International Conference on Robotics and Automation (ICRA), 2023.



Peiwen Yang received the M.S. degree in the School of Information and Electronics, Beijing Institute of Technology, Beijing, China, in 2019. He is currently a Ph.D. student in the Department of Aeronautical and Aviation Engineering, at the Hong Kong Polytechnic University.

His current research interests include aerial vehicle control, computer vision, and robotics.



Weisong Wen (Member, IEEE) received a BEng degree in Mechanical Engineering from Beijing Information Science and Technology University (BISTU), Beijing, China, in 2015, and an MEng degree in Mechanical Engineering from the China Agricultural University, in 2017. After that, he received a PhD degree in

Mechanical Engineering from The Hong Kong Polytechnic University (PolyU), in 2020. He was also a visiting PhD student with the Faculty of Engineering, University of California, Berkeley (UC Berkeley) in 2018. Before joining PolyU as an Assistant Professor in 2023, he was a Research Assistant Professor at AAE of PolyU since 2021. He has published 30 SCI papers and 40 conference papers in the field of GNSS (ION GNSS+) and navigation for Robotic systems (IEEE ICRA, IEEE ITSC), such as autonomous driving vehicles. He won the innovation award from TechConnect 2021, the Best Presentation Award from the Institute of Navigation (ION) in 2020, and the First Prize in Hong Kong Section in Qianhai-Guangdong-Macao Youth Innovation and Entrepreneurship Competition in 2019 based on his research

> REPLACE THIS LINE WITH YOUR MANUSCRIPT ID NUMBER (DOUBLE-CLICK HERE TO EDIT) <

achievements in 3D LiDAR aided GNSS positioning for robotics navigation in urban canyons. The developed 3D LiDAR-aided GNSS positioning method has been reported by top magazines such as Inside GNSS and has attracted industry recognition with remarkable knowledge transfer.



Shiyu Bai (Member, IEEE) was born in Xuzhou, Jiangsu, China. He received a Ph.D. degree in navigation, guidance, and control from Nanjing University of Aeronautics and Astronautics, Nanjing, China, in 2022. He is currently a postdoctoral fellow in the Department of Aeronautical and Aviation Engineering at the Hong Kong Polytechnic University. His research interests include inertial navigation, multi-sensor fusion, indoor positioning, and vehicular positioning.



Li-Ta Hsu (Senior Member, IEEE) received the B.S. and Ph.D. degrees in aeronautics and astronautics from National Cheng Kung University, Tainan City, Taiwan, in 2007 and 2013, respectively. He is currently an Associate Professor at the Department of Aeronautical and Aviation Engineering, The Hong Kong Polytechnic University. He is also Limin Endowed Young Scholar in Aerospace Navigation. He was a Visiting Researcher with the Faculty of Engineering, University College London, London, U.K., and the Tokyo University of Marine Science and Technology, Tokyo, Japan, in 2012 and 2013, respectively. Dr. Hsu was selected as a Japan Society for the Promotion of Sciences Postdoctoral Fellow with the Institute of Industrial Science, University of Tokyo, Tokyo, Japan, and worked from 2014 to 2016. He is an Associate Fellow with the Royal Institute of Navigation, London, U.K. He is currently a member of ION and a member of the editorial board and reviewer in professional journals related to GNSS. In 2013, he won a Student Paper Award and two Best Presentation Awards from the Institute of Navigation (ION).

His research interests include GNSS positioning in challenging environments and localization for pedestrians, autonomous driving vehicles, and unmanned aerial vehicles.